Boundary-Layer Meteorology
https://doi.org/10.1007/s10546-023-00815-z

RESEARCH ARTICLE

Turbulence Characteristics in the Atmospheric Surface Layer Over a Heterogeneous Cultivated Surface in a Tropical Region

Miriam Hounsinou[1,2] · Ossénatou Mamadou[1,2] · Basile Kounouhewa[2]

Received: 30 December 2022 / Accepted: 4 May 2023

Abstract
The description of atmospheric turbulence on heterogeneous surfaces and more specifically during stable stratification conditions, remains nowadays a relevant and open issue in micrometeorology. To partially remedy this problem, we investigate in this study, the behaviour of turbulence above a heterogeneous cultivated surface during stable and unstable conditions. The analyses were realized according to seasons using almost seven years of eddy covariance measurements acquired at 4.95 m height. The results showed that the turbulence kinetic energy per unit mass was on average less than 0.5 m^2 s^{-2} at night but increased during the day. It hits around local noon a peak value ~ 1.6 m^2 s^{-2} on average. The peak value is relatively lower (~ 0.92 m^2 s^{-2}) during the wet season compared to other periods (1.6 m^2 s^{-2}). The average value of turbulence intensities are $I_u = 0.44$, $I_v = 0.50$ and $I_w = 0.22$ following u, v, w wind speed directions. During stable conditions, there are turbulent movements when the flux Richardson number is less than a critical value estimated approximately to 0.17. The flux-variance similarity functions that characterize the behaviour of turbulence are seasonally dependent, especially under stable conditions. However, each of these functions obey the Monin–Obukhov Similarity Theory whatever the stratification except those of temperature under near-neutral conditions. The results obtained indicate that the atmospheric turbulence is relative to the type of ecosystem and the height of measurement. This process is led by aerodynamic parameters and wind speed.

Keywords Flux Richardson number · Flux-variance similarity · Heterogeneous surface · Turbulence kinetic energy · West Africa

✉ Miriam Hounsinou
miriam.hounsinou@imsp-uac.org

Ossénatou Mamadou
ossenatou.mamadou@imsp-uac.org

[1] Institut de Mathématiques et de Sciences Physiques, Université d'Abomey-Calavi, BP 613, Dangbo, Bénin

[2] Laboratoire de Physique du Rayonnement, Faculté des Sciences et Techniques, Université d'Abomey-Calavi, Abomey-Calavi, Bénin

Published online: 24 June 2023

1 Introduction

At many locations, the physical structure of the Atmospheric Boundary Layer (ABL) has changed continually during recent decades. One of the main reasons, and especially in tropical zones, is deforestation due to the expansion of cultivated areas (Lambin et al. 2003; Zeng et al. 2018, 2020; Guzha et al. 2018; FAO 2022). This transformation of natural ecosystems affects the exchanges of greenhouse gases, mass and energy which occur in the ABL (Mamadou et al. 2016; Guzha et al. 2018; Zeng et al. 2020). Knowing that these exchanges are mediated by atmospheric turbulence, understanding this turbulence remains essential to parameterize the earth-atmosphere interactions as well as to improve both regional and global climate models.

Studies related to atmospheric turbulence over cultivated areas could be of particular interest. In fact, the seasonal variability in cultivated areas, driven mainly by crop growth, make them dynamic in terms of aerodynamic parameters, which could in turn induce a seasonal dependence of the turbulent characteristics over these types of ecosystems. Moreover, the description of turbulence over heterogeneous surfaces (e.g. heterogeneous cultivated areas) is not yet well understood, contrary to homogeneous surfaces. Another issue in the ABL studies lies in the description of the turbulent processes during nighttime periods when the atmosphere is generally stable. These different challenges are related to the limits of the Monin-Obukhov Similarity Theory (MOST) which has long been used to describe the turbulent processes in the ABL. Indeed, this theory describes relatively well the atmospheric boundary layer above a flat and homogeneous surface under small stratification conditions (Foken 2017; Kaimal and Finnigan 1994; Stull 1988).

The study of turbulence structure in the stable boundary layer is of great practical importance, especially for studies related to air pollution (Mahrt 1999; Grachev et al. 2007). However, the processes that occur during stable stratification are very complex. Indeed, atmospheric observations show that with increasing stability, turbulent motions decrease, become more intermittent, then eventually disappear (Grachev et al. 2013). Under strong stable stratification, the flow is characterized by anisotropic, intermittent turbulence and wave motions of varying amplitudes and periods (Sun et al. 2015). Such a flow may not fully satisfy the usual conditions for defining turbulence (Mahrt 2014). The description of turbulent motions from flux-variance similarity functions according to MOST is therefore limited by a critical flux Richardson number Rf_c in particular under stable conditions (Grachev et al. 2013). Rf_c allows indeed distinguishing between turbulent and non-turbulent flows, but different values of Rf_c have been reported in the literature. Ellison (1957) demonstrated analytically that the flux Richardson number cannot exceed a critical value of about 0.15. However, the work of Kondo et al. (1978) on a large rice field suggests that the value of Rf_c ranges between 0.1 and 0.4. More recent studies have also revealed values within this range. This is the case of the work of Grachev et al. (2013) carried out on the Arctic pack ice during the SHEBA (Surface Heat Budget of the Arctic Ocean) experiment in the Beaufort Gyre, which showed that Rf_c is between 0.20 and 0.25. Similarly, Bou-Zeid et al. (2018) obtained $Rf_c \approx 0.21$.

Furthermore, turbulent mixing is also parameterized using Turbulence Kinetic Energy (TKE) (Babić et al. 2016a), which represents a measure of turbulence intensity. It has a keen interest in atmospheric numerical modelling (Babić et al. 2016a; Namdev et al. 2022) and in determining atmospheric dynamics and coupling (Kalapureddy et al. 2007). Sometimes, TKE is used as a starting point for turbulent diffusion approximations (Stull 1988).

In this work, turbulence is studied in a tropical region over a cultivated ecosystem using data measured from August 2007 to December 2013 by an eddy covariance system installed

in Nalohou's village, located in the northwest of Benin (West Africa). The site is not topographically complex but rather heterogeneous with varied crops. Our objective is to determine the flux-variance similarity functions and to evaluate the intensity of atmospheric turbulence at this heterogeneous site under stable and unstable conditions. To reach this objective, the scientific questions we are trying to answer are:

(1) What is the critical value of the flux Richardson number on this cultivated site?
(2) How do the similarity functions of wind speed components and scalars (temperature, humidity, CO_2) behave and what are the potential factors determining them?
(3) How do the TKE and turbulence intensity vary at the studied site?

The answers to these questions will help to identify the potential limitations of the application of MOST for a good parameterization of the atmospheric turbulence behaviour through similarity functions and turbulence intensity over a tropical cropland. The remainder of this paper is structured as follows: Sect. 2 presents the study site, the material and the data analysis; Sect. 3 describes the theoretical framework of the TKE, turbulence intensity, flux Richardson number and the Monin–Obukhov similarity; Sect. 4 presents the results and discussion; and finally Sect. 5 offers the conclusion.

2 Site and Data Used

2.1 Study Site

The Nalohou site (9.74° N, 1.60° E, 449 m) is located in north-western Benin in West Africa, in the Donga watershed, which occupies 586 km^2 of the area. Nalohou lies in a tropical region characterized by a dry and a wet (or rainy) seasons separated by transitional phases (moistening and drying). The length of the seasons varies year to year. From 2007 to 2013, the dry season usually begins in late December and lasts on average less than 2 months. The wet season is longer, approximately 6 months. It often starts in April and ends in October.

The site area is flat with a slope lower than 3% and the vegetation cover is dynamic; one can find a succession of different crops interspersed with a fallow period. During the wet seasons, different types of crops are planted. The main food crops produced on the site are yams, cassava, and maize. There are also some cash crops, such as cotton and cashews. The soil is almost bare during the dry season, while grass completely covers it during the fallow periods. More details about the site can be found in Guyot et al. (2012); Mamadou et al. (2014) and Ago et al. (2014).

2.2 Meteorological and Eddy Covariance Data

Meteorological sensors have been installed on the site since 2005 for the measurement of air temperature, humidity, pressure, radiation, wind speed and direction at 2 m height, soil temperature at several depths (10, 20, 40 cm) below the surface and rainfall. These sensors operate at a low frequency and data are averaged to the half-hour.

High frequency measurements (20 Hz) started in August 2007 with a sonic anemometer (CSAT3 Campbell Scientific, Logan (UT) USA) which allows to obtain the three components of wind speed (u, v, w) and the sonic temperature, and with an open path gas analyzer (LI-7500, LI-COR, Lincoln (NE), USA) for the measurements of CO_2 and water vapour concentrations. These sensors are placed at a height of 4.95 m and the data acquired after processing are averaged over a time interval of 30 min. Several corrections (peak suppression,

double rotation, sonic - Licor time lag correction, density correction for sonic temperature, spectral and Webb corrections) are applied to the high frequency data with the EdiRe software (version 1.5.0.28, University of Edinburgh). The 'block de-trending' has been used to obtain fluxes as well as all velocity variances used in this study.

To characterize the atmospheric turbulence in our study, some filters were applied to the half-hourly data:

- All data measured during rainy events were discarded since the licor used was open-path.
- The data of the covariance between vertical wind speed fluctuations w' and those of the longitudinal wind speed component u', temperature T', humidity q' and CO_2 concentration c' ($\overline{w'u'}$, $\overline{w'T'}$, $\overline{w'q'}$ and $\overline{w'c'}$), were excluded when judged to be non-stationary using the test proposed by Foken and Wichura (1996) with a critical value of 30%.
- The standard deviations data of wind speed components $\sigma_{u,v,w}$ and temperature σ_T acquired by the sonic anemometer when there is no turbulence were rejected for absolute values of sensible heat flux lower than 10 W m^{-2}. Similarly, the standard deviation data of air humidity σ_q were filtered when |LE| (absolute value of latent heat flux) is lower than 5 W m^{-2}. Finally, the night-time data of σ_c (standard deviation data of CO_2) for which the friction velocity $u* < 0.1$ m s^{-1} (Ago et al. 2014) were discarded from the dataset.

The analyses were done in the Monin–Obukhov's stability parameter ζ interval of -2 to 2. Especially for the determination of the flux-variance similarity functions, a more rigorous filter was applied to data when (1) the mean wind speed (U) is less than 1 m s^{-1} for all stratifications and (2) the flux Richardson number is higher than its critical value Rf_c in stable conditions only; this is to get rid of data measured in non-turbulent conditions. The extreme peaks of the normalized data of standard deviations of wind speed components and atmospheric scalars data were also discarded. Finally, the standard deviation data for each of the wind speed components normalized by the friction velocity retained were 27402 in the unstable condition and 5223 in the stable condition. Those of temperature, humidity and carbon dioxide concentration normalized by each of their appropriate scale parameters were 26863, 22418, 23293 in unstable condition and 5224, 4473, 6064 in stable condition, respectively.

3 Methodology

3.1 Turbulence Kinetic Energy and Turbulence Intensity

Turbulence Kinetic Energy (TKE) is one of the most important quantities used to study the turbulent atmospheric boundary layer (Stull 1988). It is directly related to the transport of momentum, heat, and mass in the boundary layer (Stull 1988) and provides information about the energy content of eddies (Rodrigo and Anderson 2013). The TKE budget equation with each of these individual terms describing the physical processes that generate and dissipate turbulence is given by Eq. 1 from Stull (1988). The relative balance of these processes determines the ability of the flow to maintain turbulence or to become turbulent, thus indicating its stability state (Stull 1988):

$$\underbrace{\frac{\partial e}{\partial t}}_{I} + \underbrace{\overline{U_j}\frac{\partial e}{\partial x_j}}_{II} = \underbrace{\delta_{i3}\frac{g}{\overline{T}}\overline{u_i' T'}}_{III} - \underbrace{\overline{u_i' u_j'}\frac{\partial \overline{U_i}}{\partial x_j}}_{IV} - \underbrace{\frac{\partial \overline{u_j' e'}}{\partial x_j}}_{V} - \underbrace{\frac{1}{\overline{\rho}}\frac{\partial \overline{u_i' p'}}{\partial x_i}}_{VI} - \underbrace{\varepsilon}_{VII}. \tag{1}$$

The terms *I–VII* represent the local storage, advection, buoyant production or consumption, mechanical or shear production, turbulent transport, pressure correlation and dissipation of TKE, respectively. We note g the gravitational acceleration, ρ the air density, p the pressure and e the TKE per unit mass. The latter is defined by:

$$e = \frac{1}{2}\left(\overline{u'^2} + \overline{v'^2} + \overline{w'^2}\right) = \frac{1}{2}\left(\sigma_u^2 + \sigma_v^2 + \sigma_w^2\right). \tag{2}$$

By scaling Eq. 2 by the square of the friction velocity ($u*^2$), one can notice that turbulent kinetic energy is linked to the standard deviation of wind speed components normalized by $u*$ as follows:

$$\frac{e}{u_*^2} = \frac{1}{2}\left[\left(\frac{\sigma_u}{u_*}\right)^2 + \left(\frac{\sigma_v}{u_*}\right)^2 + \left(\frac{\sigma_w}{u_*}\right)^2\right]. \tag{3}$$

The turbulence intensity for longitudinal u, transverse v and vertical w directions is given by:

$$I_{i=u,v,w} = \frac{\sigma_i}{U}. \tag{4}$$

3.2 Flux Richardson Number

An appropriate measure of stability is also necessary to study processes which occur in the ABL. Indeed, the latter responds to changes in stability caused by either the heating or the cooling of soil (Kaimal and Finnigan 1994). The flux Richardson number (*Rf*) is, according to Kaimal and Finnigan (1994), a good measure of stability effects in the surface layer. *Rf* is defined as the ratio of buoyancy production or consumption (term *III* of Eq. 1) to shear production (term *IV* of Eq. 1) of the TKE budget:

$$Rf = \frac{\frac{g}{T_v}\overline{w'T'}}{\overline{w'u'}\left(\frac{\partial U}{\partial z}\right)}; \tag{5}$$

where T_v is the virtual temperature. In the case where we have only wind speed measurements at a single altitude (such as the case of this study), the profile or vertical gradient of wind speed ($\partial U/\partial z$) can be estimated using the bulk difference between the measurement height z and $d + z_0$ (Eq. 6) where $U(d + z_0) = 0\ m\ s^{-1}$ with z_0 the roughness length and d the displacement height in the zero plane (Foken 2017):

$$\frac{\partial U}{\partial z} = \frac{U(z) - U(d + z_0)}{z - (d + z_0)}. \tag{6}$$

Several methods for estimating these aerodynamic parameters (d and z_0) are proposed in the literature (Brutsaert 1982; Rotach 1994; Martano 2000; Toda and Sugita 2003; Tsai and Tsuang 2005; Kent et al. 2017). In this study, d has been computed using the relationship:

$$d = \frac{2}{3}h_{veg}, \tag{7}$$

proposed by Brutsaert (1982) while z_0 was determined using:

$$z_0 = 0.17 + 0.097 h_{veg}, \tag{8}$$

established by Mamadou et al. (2014), where h_{veg} is the vegetation height.

During stable stratification, Rf provides information on the development of turbulence from its critical value above which the airflow is or becomes laminar, i.e., dynamically stable (Stull 1988; Foken 2017). Otherwise, the flow is dynamically unstable or turbulent.

According to Grachev et al. (2013), the turbulent to non-turbulent flow transition problem does not have a rigorous mathematical resolution. From the equations for turbulent energy, the mean square temperature fluctuation and the covariance of temperature and vertical velocity, with some speculative hypotheses about the dissipative action of turbulence, Ellison (1957) had shown that the transition condition from turbulent to laminar flow is associated to a critical flux Richardson number. Similarly, experimental studies have shown that Rf is a monotonically increasing but bounded function of Ri or ζ in stable condition (e.g., see Fig. 3 of Rogachevskii et al. (2021) and Fig. 7 of Babić et al. (2016a)). There is thus a finite asymptotic value of Rf (Freire et al. 2019) above which the flow is not well turbulent. This value was determined in this study from the distribution of Rf with respect to ζ.

3.3 Monin–Obukhov Similarity Theory

Atmospheric turbulence in the ABL is studied by the Monin–Obukhov Similarity Theory (MOST), also known as surface-layer similarity using the flux-gradient and flux-variance similarity functions obtained by dimensionless analysis (Stull 1988; Kaimal and Finnigan 1994; Foken 2017). The flux-variance similarity functions are the standard deviations normalized (by the appropriate scaling parameters) of the components of wind speed (u, v, w), temperature T, humidity q, and carbon dioxide concentration c, all defined as functions of the atmospheric stability parameter ζ:

$$\begin{cases} \phi_i(\zeta) = \frac{\sigma_{i=u,v,w}}{u_*} \quad with \quad u_* = \sqrt{|-\overline{u'w'}|}, \\ \phi_i(\zeta) = \frac{\sigma_{i=T,q,c}}{x_*} \quad with \quad x_* = -\frac{\overline{w'x'}}{u_*}. \end{cases} \tag{9}$$

The expression of ζ is given by:

$$\zeta = \frac{z-d}{L} \quad with \quad L = -\frac{u_*^3 T_v}{\kappa g \overline{w'T'}}, \tag{10}$$

where κ is the von Karman constant.

The expressions for these universal functions of ζ are not predicted by MOST and must be determined empirically. They are, for example, often expressed as Eq. 11 (Kaimal and Finnigan 1994; Moraes et al. 2005; Fortuniak et al. 2013; Nadeau et al. 2013):

$$\phi_i(\zeta) = \alpha_i (1 + \beta_i \zeta)^{\gamma_i}; \tag{11}$$

where α_i, β_i and γ_i are empirical coefficients. In this work, the expressions for $\phi_i(\zeta)$ are determined by the least squares method using the Mosaic package on R (version 4.1.0) software.

Note that the $\phi_i(\zeta)$ relationships can be influenced by self-correlation effects induced by u_* lying on both sides in Eq. 9 (Klipp and Mahrt 2004; Babić et al. 2016a, b). The degree of self-correlation is evaluated in this study following the approach proposed by Klipp and Mahrt (2004). This consists of simulating 1000 random datasets using the real observation data as

a base value from which random sampling with replacement are made (Klipp and Mahrt 2004). Indeed, for each simulated random data set, each of the variables (σ_i, u_*, $\overline{T}$, $\overline{w'T'}$, $\overline{w'q'}$ et $\overline{w'c'}$) implicated in Eq. 9 is redistributed randomly with replacement independently of the other variables. New values of $\phi_{i\,random}$ and ζ_{random} are determined and the linear correlation coefficient between them is calculated. The average of the linear correlation coefficients between $\phi_{i\,random}$ and ζ_{random} from the 1000 simulations represents a measure of self-correlation since the random data no longer have any physical significance (Klipp and Mahrt 2004; Nadeau et al. 2013; Babić et al. 2016b). The actual fraction of variance explained by physical processes is thus given by ${R_{dif}}^2$,

$$R_{dif}^2 = R_d^2 - R_r^2. \tag{12}$$

R_d is the linear-correlation coefficient for the original data and R_r is the average correlation coefficients for 1000 trials of random data.

4 Results and Discussion

4.1 Climatic Conditions Prevailing at the Study Site

The temporal dynamic of the meteorological variables allows appreciation of the evolution of the atmospheric boundary layer during the studied period. Figure 1 illustrates the variation of the stability parameter and other meteorological variables (incoming short-wave radiation, air and soil temperatures). The seasonal variations of wind roses by atmospheric stability are presented in Fig. 2. The atmosphere is generally stable ($\zeta > 0$) at night and unstable ($\zeta < 0$) during the day at the study site (Fig. 1b). In the region where the study is performed, the dry season is marked by the harmattan winds, where northeasterly winds loaded with dry and hot air masses, but less hot at night (Fig. 1c), come from the Sahara (Afeti and Resch 2000; Lothon et al. 2008). An inversion of the wind direction is observed during the West African monsoon. The increase of air temperature (Fig. 1c) due to insolation from January to March (Fig. 1a) induces a convection between the continent (hot) and the ocean (cold), leading to episodes of humid southwestern winds coming from the Gulf of Guinea and resulting in rainy season.

The beginning and the end of seasons were identified in this study based on wind direction and absolute air humidity (q_a) (Mamadou 2014; Mamadou et al. 2014), which take into account synoptic changes and microclimatic conditions, respectively (Lothon et al. 2008; Doukouré 2011). Then, the q_a thresholds of 6 and 16 g m^{-3} were used to delimit the length of dry and wet seasons, respectively. Indeed, based on the relationship between wind direction and absolute humidity, Mamadou (2014) found that the q_a thresholds allow disentangling northeast and southwest winds. The moistening (drying) phase which precedes the wet (dry) season has then absolute air humidity values between 6 and 16 g m^{-3}. It is important to note that these thresholds were not applied to the half-hourly humidity data but to their 20 days sliding window (Mamadou 2014).

For the 2007–2013 period, Fig. 2 shows that the dominant winds are from the northeast direction during the dry season, whereas during the wet season we observe mostly southwest winds regardless of the stratification of the atmosphere. The wind speed is generally less than 3 m s^{-1} with an occurrence of relatively stronger winds up to ~ 6 m s^{-1} in unstable conditions and especially during the dry season (Fig. 2). The air temperature (Tair) is 28.30 ± 3.2 °C (median value ± semi-interquartile range) in unstable condition and 23.21 ± 2.04 °C

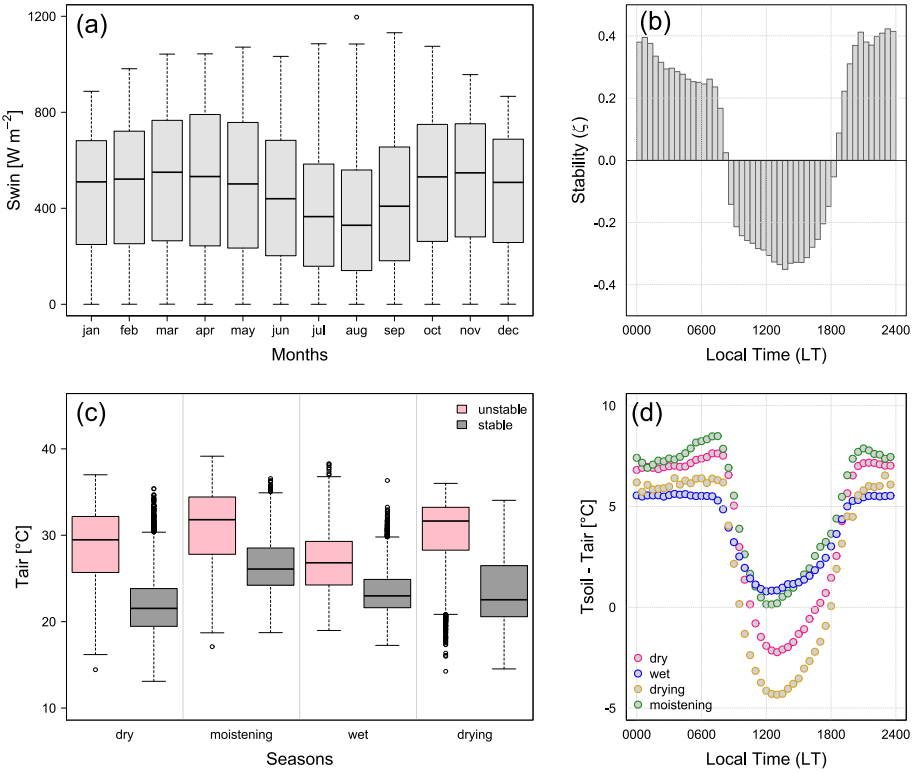

Fig. 1 Boxplot of the distribution of Swin as a function of months (**a**), diagram of the mean diurnal cycle of the stability parameter ζ (**b**), Boxplot of the distribution of air temperature according to seasons and stability condition (**c**) and mean diurnal cycle of the difference between soil and air temperature according to seasons (**d**), observed from August 2007 to December 2013 at the Nalohou site

in stable condition, with a median value of incoming shortwave radiation (Swin) received between 0630 and 1800 LT (local time = UTC + 1 h), of 473 W m^{-2} (Fig. 1a) and an annual precipitation accumulation ranging from 934 (obtained in 2011) to 1470 mm (obtained in 2010). The soil temperature (Tsoil) at 10 cm depth on average equals 29.54 ± 3.98 °C in unstable condition and 29.39 ± 3.35 °C in stable condition (Fig not shown) and is higher than the air temperature (δT = Tsoil − Tair > 0). However, during the dry season and the drying period, Tsoil < Tair approximatively between 1000 and 1800 LT (Fig. 1d). This finding can be explained by the high incoming solar irradiance during these time slots and the low relative humidity during these periods (dry season and drying period) of the year. Indeed, the wind roses show that during the periods when Tair > Tsoil the dominant winds come from the northeast direction, which corresponds to the harmattan winds. In addition, Mamadou et al. (2014) highlighted a dampening effect of the outgoing longwave radiation related to the presence of vegetation (fallow) of almost 3 m height at the site, especially during the drying period.

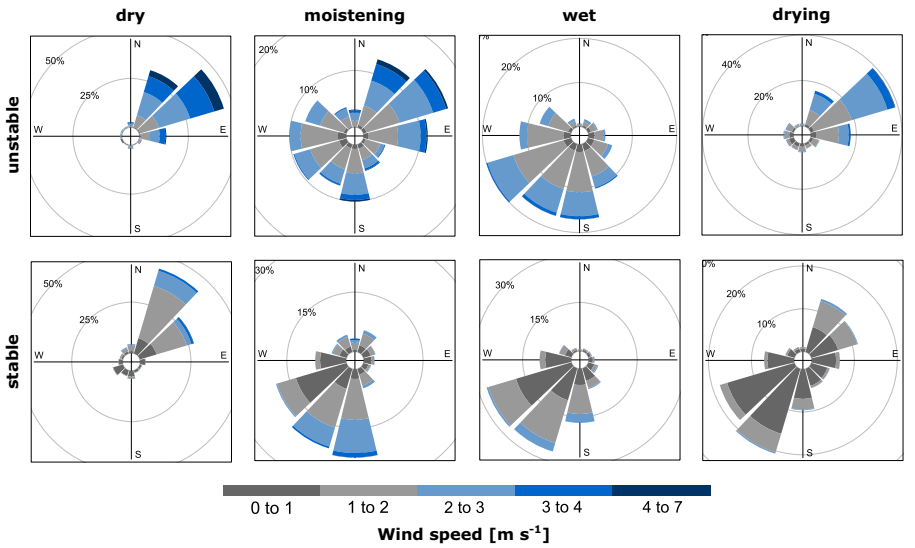

Fig. 2 Wind roses observed in stable and unstable conditions during each season and transition phases at the Nalohou site. The colors darkgray, gray, lightblue, blue and darkblue represent wind speeds between 0–1, 1–2, 2–3, 3–4 and 4–7 m s^{-1}, respectively

4.2 Surface conditions, Footprint Analysis and Turbulent Fluxes

The Aerodynamic parameters (z_0 and d) that characterize the study site have been estimated using Eqs. 7 and 8, and the vegetation height (h_{veg}) data were simulated using the Anterior Precipitation Index (API) model (Pellarin et al. 2009; Mamadou 2014). Indeed, the determination of h_{veg} is based on a hypothesis that vegetation growth is essentially related to the water available in the soil and that the API needs only precipitation data as model input to provide soil moisture (Pellarin et al. 2009). The h_{veg} is manually reset ($h_{veg} = 0$ m) on the burning date, which often happens during the drying period. In this period, measurements might be too close to the canopy when $h_{veg} > 2.5$ m as suggested by Aubinet et al. (2012) but h_{veg} is generally less than 3 m on the site.

The estimation of z_0 and d during the years 2007–2013 are presented in Fig. 3, which shows an ascending growth of z_0 and d each year and an inter-annual variation especially between April and November, the growing period of plants. This result is naturally explained by the relatively distinctive development of different types of crops and herbaceous fallow. During the dry season, the soil is almost bare ($d = 0$ m) and the roughness length is very small ($z_0 = 0.17$ m) relative to the wet season and transitional periods, during which the soil is covered with various crops and herbaceous fallow ($d \neq 0$ m) and z_0 varies from ~ 0.17 to ~ 0.46 m (Fig. 3).

The contribution area to the measured fluxes (footprint) during the different seasons and transition phases under both stability conditions are shown in Fig. 4. The footprints were computed with the two-dimensional parameterisation Flux Footprint Prediction (FFP) model (Kljun et al. 2015) with the estimated data of aerodynamic parameters (d and z_0) and other variables (wind speed and direction, Obukhov length, standard deviation of the lateral component of the wind speed, friction velocity and measurement height). The analysis reveals that the major directions of flux contribution measured during seasons/transition phases (Fig. 4)

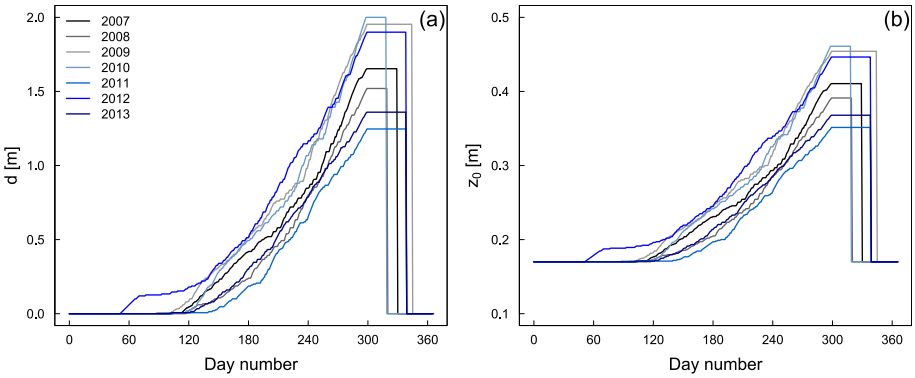

Fig. 3 Inter-annual variation in displacement length (**a**) and roughness height (**b**) obtained over the Nalohou site

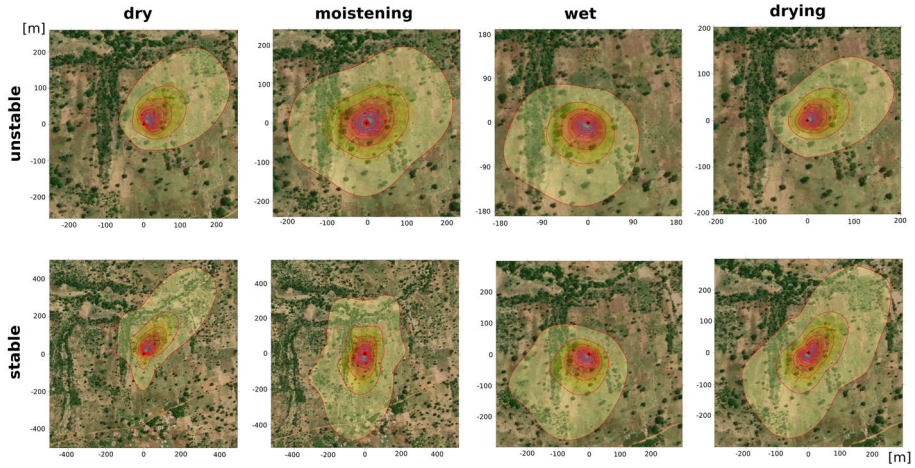

Fig. 4 Footprint climatology for Nalohou station for each season and transition phases under unstable and stable condition. The black "+" depicts the mast location. Footprint contour lines are shown from 10 to 90% with an interval of 10%

are in accordance with the dominant wind directions observed during each season/transition phase (Fig. 2). Under stable conditions, the footprint area is about twice as large as the footprint area under unstable conditions, especially during the dry season and the moistening phase of the atmosphere. However, in the wet season, it is smaller relative to the other periods (Fig. 4). Overall, during all seasons, isolines (from 10 to 70% of the total surface considered) which mostly contributed to measured fluxes are composed of crop area and some isolated shrubs. Some contributed sources (80–90%) appear from a riparian forest located ~ 100 m near the flux tower.

Momentum (τ), sensible heat (H), latent heat (LE), and carbon dioxide (Fc) fluxes measured at the Nalohou site as a function of ζ are presented in Fig. 5. The seasonal diurnal cycles of each of these fluxes are also illustrated (Fig. 5). All fluxes in absolute values ($|\tau|$, |H|, |LE| and |Fc|) reach their maximum when $0 > \zeta > -0.5$, that is, under unstable and near-neutral

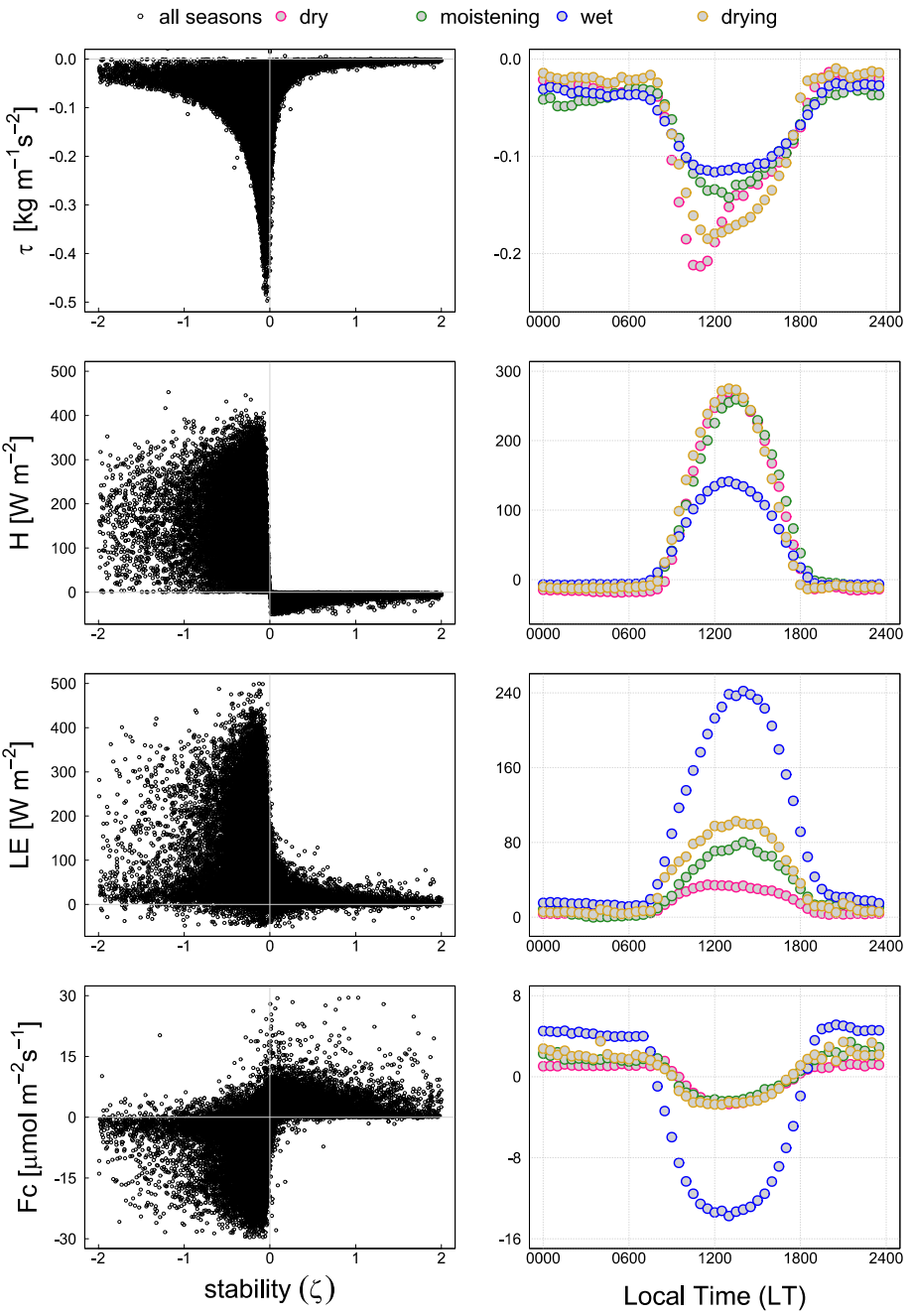

Fig. 5 The variations of momentum (τ), sensible heat (H), latent heat (LE), and carbon dioxide (Fc) fluxes with respect to the stability parameter ζ and the average diurnal cycles of these fluxes. The black circles represent the measurements for all seasons. The lightgray points with pink, green, blue and gold borders represent the hourly averages of fluxes in dry, moistening, wet and drying seasons, respectively

conditions. H and LE fluxes vary between − 50 and 400 W m^{-2}; − 0.5 < τ < 0 kg m^{-1} s^{-2} and − 30 < Fc < 20 μmol m^{-2} s^{-1}. The average diurnal cycles of fluxes show that those obtained in the wet season (blue points) are particularly different from those measured during the other periods. In the wet season, there is both a higher emission (absorption) of CO_2 and actual evapotranspiration during the night (day) compared to other seasons because of the presence of growing crops and a relatively denser vegetation in the footprint area. Conversely, H is lower compared to other seasons due to the thermodynamic conditions (lower air and soil temperatures) (Fig. 1c), and the lowest magnitude of |τ| can be attributed to that of wind speed (Fig. 2). This is because higher wind speeds induce a larger momentum flux (Wang et al. 2016). However, it is the combined action of wind speed and underlying surface roughness that determines τ (Wang et al. 2016). This flux is more associated to the development of mechanical turbulence, which explains its lower nighttime values (stable stratification) (Fig. 5) since the turbulence is not well developed (Aubinet et al. 2012).

Under unstable conditions, the sensible heat flux is upward from the surface to the atmosphere (H > 0 W m^{-2}) due to solar radiation. In stable conditions, the radiative cooling of the soil due to sunset leads to a downward sensible heat flux (H < 0 W m^{-2}).

4.3 Flux-Variance Similarity and Critical Flux Richardson Number

4.3.1 Relationship Between the Normalized Standard Deviations of the Vertical Wind Speed Component and Wind Direction

In order to examine whether there are flow disturbances in any wind direction, we have illustrated in Fig. 6 the normalized standard deviation of the vertical component of wind speed ($\sigma_w/u*$) as a function of wind direction when the atmosphere is near neutrality (− 0.05 < ζ < 0.05). According to MOST, $\sigma_w/u*$ must be constant near neutrality while Panofsky and Dutton (1984) suggested a value of ~ 1.25 over an "ideal" terrain for this ratio.

In this study, we found when − 0.05 < ζ < 0.05 that $\sigma_w/u*$ varies between 1.1 and 1.5 as a non-monotonic function with respect to wind direction in the wet season and during transition periods, whereas during the dry season $\sigma_w/u*$ is similar to a nearly constant function on average equal 1.20 ± 0.08 (Fig. 6). It could be thus deduced that the wind circulation seems not to have been disturbed during the dry season where the soil is almost bare, contrary to the wet season and transition periods where the soil is covered with heterogeneous vegetation that may affect the air flow. However, the wind direction varies less between 0° and 70° in the dry season compared to the other seasons. It is also noted that σ_w/u_* shows similar variation in this wind sector (~ 0° to 70°) during other periods than the dry season. This means that the airflow is probably not disturbed in this sector. On the other hand, the change of the agricultural area at the riparian forest in the wind sector ~ 60° to 240° (see Fig. 4) may influence the airflow in this sector. This could explain the variations of σ_w/u_* between ~ 60° and 240° (Fig. 6) since σ_w/u_* becomes almost constant (regardless of the season) in the wind sector ~ 240° to 300°, then increases to between 300° and 330° where the small tree cluster is located (see Fig. 4). We can finally summarize that σ_w/u_* is influenced by a directional effect of wind associated with the large-scale heterogeneity of the canopy in the footprint area.

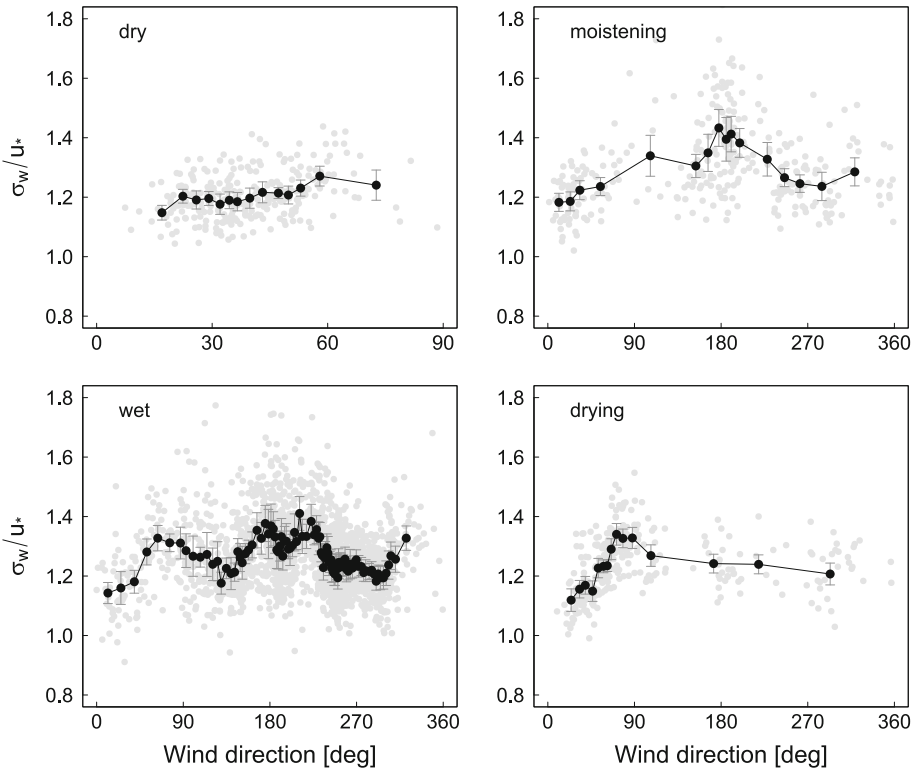

Fig. 6 Relationship between the normalized standard deviations of the vertical wind speed component as a function of wind direction during near-neutral stratification **(|ζ|< 0.05)**. The black points represent the bin-averages (of 20 individuals) of the gray points and the error bars represent the 95% confidence intervals on the averages

4.3.2 Critical Flux Richardson Number

Figure 7 shows the dependence of Rf with respect to ζ. Rf admits a finite asymptote at $Rf = Rf_c \approx 0.17$ when $\zeta \rightarrow +\infty$ (Fig. 7). This critical value is an approximation of the actual critical value of the flux Richardson number since the latter was calculated using approximate values of the wind speed gradient. The approximation for the wind speed gradient is likely to be a better estimate close to the critical Richardson number since the wind shear tends to vary less strongly with height in very stable conditions. However, this approximation seems logical because the critical value obtained is in accordance with the results obtained by Arya (1972) and Kondo et al. (1978), who found, respectively, $Rf_c = 0.15$–0.25 using the equations of Reynolds stress and turbulent energy and $Rf_c = 0.1$–0.4 over a rice field. Besides, Grachev et al. (2013) explain that some small-scale turbulence occurs in the $Rf > Rf_c$ regime, which is not a Kolmogorov turbulence. The data measured in these conditions could thus bias the results of the similarity functions under stable conditions. This is the case of the study done by Pahlow et al. (2001) and re-analyzed by Basu et al. (2006). The latter have removed non-turbulent effects from the data used in Pahlow et al. (2001) work with discrete wavelet transforms to demonstrate that the conclusion drawn by Pahlow et al.

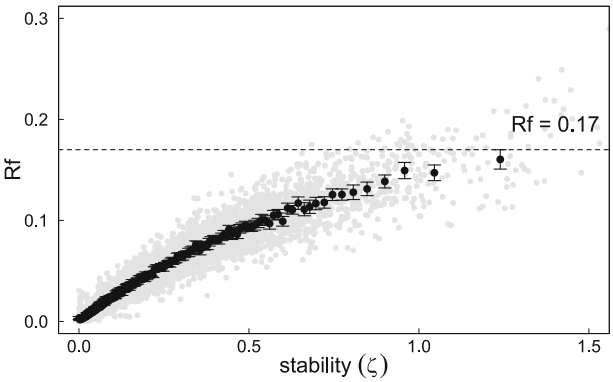

Fig. 7 Variation of flux Richardson number *Rf* with respect to the stability parameter ζ. The black points represent the bin-averages of 40 individuals of the gray points and the error bars represent the 95% confidence intervals on the averages

(2001) regarding the invalidity of z-less stratification for σ_u/u_* under very stable conditions is biased by the inclusion of non-turbulent motions.

4.3.3 Similarity Functions

The expressions of the similarity functions were determined for each season and each transition phase in stable and unstable conditions. Note that the observations of σ_T/T_*, σ_q/q_* and σ_c/c_* were not taken into account during the fitting for $\zeta \in [-0.01, 0.01]$, $\zeta \in [-0.05, 0.05]$ and $\zeta \in [-0.05, 0.05]$, respectively, due to the large dispersion of these ratios over these intervals. Figure 8a and b show the distributions of these ratios as a function of ζ and their fitted curves.

The σ_u/u_*, σ_v/u_* and σ_w/u_* are on average equal to 2.31 ± 0.37, 2.45 ± 0.49 and 1.26 ± 0.12, respectively, in near-neutral condition and increase very little with ζ in stable condition (Fig. 8a). These values in near-neutral condition (except for σ_v/u_*) are close to those expected ($\sigma_v/u_* = 2.39$, $\sigma_w/u_* = 1.25$) for horizontally homogeneous and flat field (Panofsky and Dutton 1984). Under unstable condition, $\sigma_{u,v,w}/u_*$ increase as ζ decreases and reach around double their amplitudes under stable conditions (Fig. 8a). However, a seasonal variation of all similarity functions was observed at the study site, notably under stable conditions (Fig. 8a, b). Nevertheless, each of the similarity functions obtained respects the Monin–Obukhov similarity theory whatever the season/transition phase and the stratification of the atmosphere, except σ_T/T_*, which is a function of ζ to the power − 1 when $-0.08 < \zeta < 0.1$ (Fig. 8b).

The comparison of models obtained in this study with those available in litterature and especially in tropical regions (Moraes et al. 2005; Lohou et al. 2010; Hounsinou et al. 2022) reveal differences but some similarities were noted (Fig. 8a, b). The variation of $\phi_w(\zeta)$ when $\zeta < 0$ (Fig. 8a) and that of $\phi_T(\zeta)$ when $\zeta < -0.1$ (Fig. 8b) are close to those of Lohou et al. (2010) on a glade surrounded by woodland, crops and fallow in northern Benin. Likewise, that of $\phi_v(\zeta)$ in the dry season is close to the model obtained by Moraes et al. (2005) on a rice field located in an alpine area in southern Brazil when $-10^{-1} < \zeta < -10^{-2}$ (Fig. 8a). Moreover, the seasonal dependence of similarity functions observed in this study has been also noted previously by Hounsinou et al. (2022) over a woodland forest

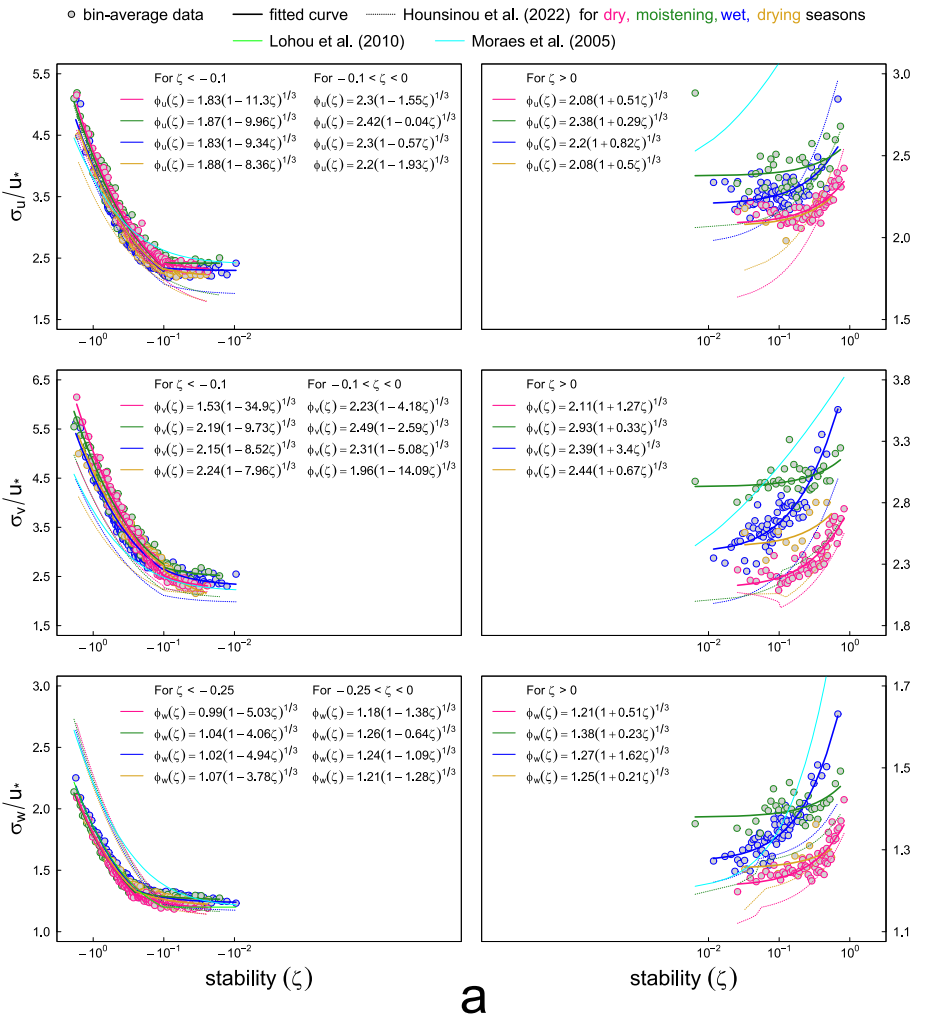

Fig. 8 a The normalized standard deviations of wind speed components as functions of ζ under unstable and stable conditions and **b** the normalized standard deviations of atmospheric scalars as functions of ζ under unstable and stable conditions. The lightgray points with pink, green, blue and gold borders represent the bin-averages (of 30 individuals) of the 30 minutes measurements in dry, moistening, wet and drying seasons, respectively. The pink, green, blue and gold solid curves represent the models established in this study for the dry, moistening, wet and drying seasons, respectively. The expressions of the fitting models obtained are written on the figures. The lightgreen curves represent the Lohou et al. (2010) models, the cyan curves represent the Moraes et al. (2005) models and those established by Hounsinou et al. (2022) are represented by the pink, green, blue and gold dashed curves for the dry, moistening, wet and drying seasons, respectively

(Fig. 8a, b). But seasonally, the similarity functions of the woodland forest differ from those established herein. Indeed, the forest site is located 13 km apart from the heterogeneous site involved in this study. Weather conditions of these two sites were not significantly different as already demonstrated by Mamadou et al. (2016), who had compared two annual cycles (from July 2008 to June 2010) of meteorological variables (incoming short-wave radiation, air temperature and vapour pressure deficit (VPD)), soil water content and leaf area index

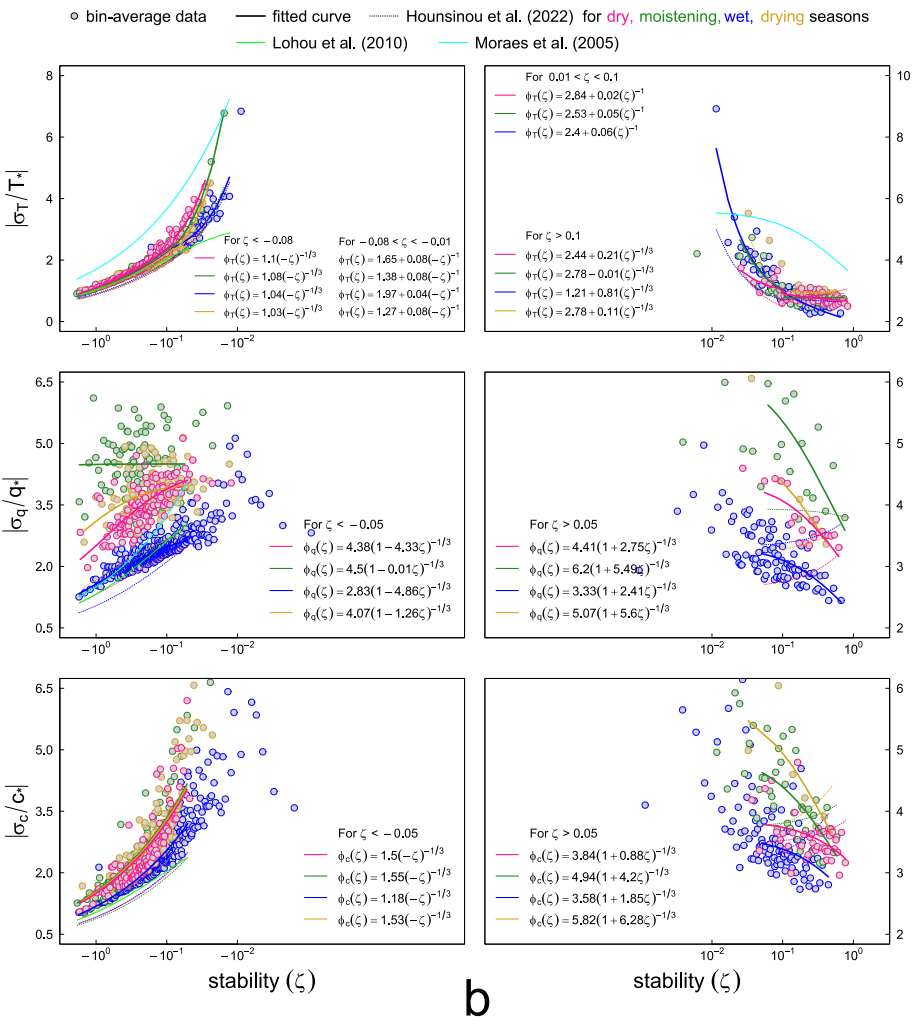

Fig. 8 continued

(LAI). However, major differences have been evidenced, as expected, in LAI and soil moisture dynamics (see Fig. 2 in Mamadou et al. (2016)). Hence, we hypothesize that aerodynamic parameters would be the main factors which determine the flux-variance similarity functions. Also, these ratios could depend on the measurement height since they were acquired at the forest at 18 m height while at the culture site they were taken at 4.95 m. The relative impact of the measurement height on the similarity models had been indeed suggested by Liu et al (2017), who made a comparative study of all flux-variance similarity functions at several altitudes over the city of Beijing, China. In addition, the results obtained by Hurdebise et al. (2017) over a forest in Belgium have shown that the efficiency of momentum transfer depends on the difference between the measurement height z and the displacement height d.

Moreover, $\sigma_w/u*$ depends on the wind direction during quasi-neutral conditions (Fig. 6) and all similarity functions depend on the seasons, especially under stable conditions.

Table 1 Results of self-correlation assessment for all flux-variances similarity functions

	ϕ_u	ϕ_v	ϕ_w	ϕ_T	ϕ_q	Φ_c
R_d						
$\zeta < 0$	− 0.724	− 0.729	− 0.761	0.451	0.028	0.215
$\zeta > 0$	0.16	0.181	0.228	− 0.191	− 0.017	− 0.04
R_r						
$\zeta < 0$	− 0.361	− 0.352	− 0.381	0.079	0.064	0.039
$\zeta > 0$	0.105	0.107	0.225	− 0.03	− 0.018	0.012
${R_{dif}}^2$						
$\zeta < 0$	0.394	0.407	0.434	0.198	− 0.003	0.045
$\zeta > 0$	0.014	0.021	0.001	0.036	0	0.001

Knowing that changes in the wind direction lead to that of the season, one can finally argue that there is a directional effect of wind on the flux variance similarity functions, especially under stable condition.

4.3.4 Self-correlation Analysis

The results of the self-correlation assessment are shown in Table 1. The linear correlation coefficient R_d between the real observation data of the normalized standard deviations $\sigma_{u,v,w,T,q,c}$ and the stability parameter ζ varies between − 0.76 and 0.45 depending on the variable and stability conditions (Table 1). As for the correlation of the randomized data R_r, which represents therefore a measure of the self-correlation, it varies between − 0.38 and 0.22 acccording to the variable and the stratification (Table 1). The $\sigma_{u,v,w}/u_*$ appear to be more correlated with ζ, compared to $\sigma_{x=T,q,c}/x_*$. Similarly, the self-correlation is more significant for $\phi_{u,v,w}(\zeta)$ than for $\phi_{T,q,c}(\zeta)$. However, the real fraction of variance explained by physical processes is larger (${R_{dif}}^2 \approx 0.4$) for $\phi_{u,v,w}(\zeta)$ than for $\phi_{T,q,c}(\zeta)$ (${R_{dif}}^2 \leq 0.2$) when $\zeta < 0$, but ${R_{dif}}^2$ does not show a particular difference between all analyzed variables when $\zeta > 0$.

Considering that the values of ${R_{dif}}^2 > 0.2$ cannot be explained by self-correlation and must have a physical reason (Barskov et al. 2022), we can argue that the similarity functions $\phi_{u,v,w}(\zeta)$ and $\phi_T(\zeta)$ in the unstable condition can be explained by physical turbulence processes even if they are influenced by self-correlation effects induced by u_*. In general, the self-correlation is more significant in the unstable condition compared to the stable condition for all variables, but the real fraction of variance explained by physical processes is larger in the unstable condition except for $\phi_q(\zeta)$. The self-correlation has a significant impact on the total variance of $\phi_q(\zeta)$ in the unstable condition since ${R_{dif}}^2 < 0$. This suggests that q_* does not seem to be an appropriate scaling parameter in this stratification. Moreover, this could be a limitation of the method of evaluating the self-correlation effect itself since the self-correlation and the physical correlation may not be linear (Klipp and Mahrt 2004).

4.4 Turbulence Kinetic Energy

The evolution of TKE per unit mass scaled by the square of the frictional velocity (e/u_*^2) with respect to ζ at the Nalohou site is shown under both stratifications in Fig. 9a. Under stable conditions when the prevailing winds are from the northeast, e/u_*^2 averages 6.86 and 6.24 during the drying phase and dry season, respectively. In contrast, it is relatively higher

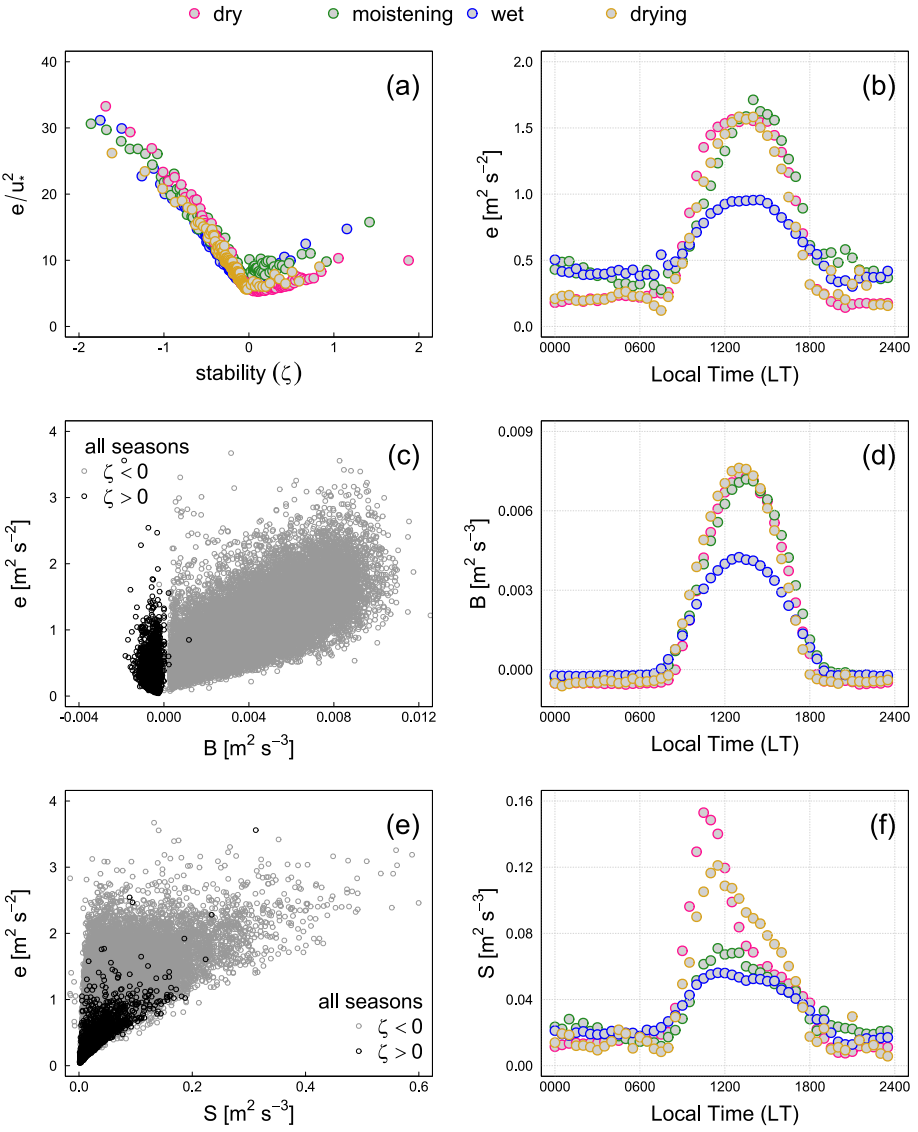

Fig. 9 Variation of TKE per unit mass normalized with respect to stability (**a**), variation of TKE per unit mass with respect to Buoyant production or consumption $B = \frac{g}{T}\overline{w'T'}$ (**c**) and with respect to Shear production $S = -\overline{u'w'}\frac{\partial \overline{U}}{\partial z}$ (**e**), average diurnal cycle of TKE per unit mass (**b**), buoyancy term (**d**) and shear term (**f**)

(9.12 during the moistening phase and 7.57 in the wet season) when the southwest winds are prevailing. However, under unstable condition, e/u_*^2 decreases from ~ 33 to ~ 6.5 when $-2 < \zeta < -0.1$ and becomes almost constant when ζ tends to 0.

e/u_*^2 increases rapidly as ζ becomes lower following the variation of the individual $\sigma_{u,v,w}/u_*$ values in Fig. 8a and e has a strong diurnal cycle (see Fig. 9b), consistent with the diurnal cycle of stability. The cycle shows that e during the night time is averages less than 0.5 m^2 s^{-2} but begins to increase during the day with sunrise and the occurrence of relatively stronger winds to reach its maximum around 1300–1500 LT, and then decreases with time until sunset. The average maximum value of e obtained at the site was ≈ 1.6 m^2 s^{-2} but it is relatively lower in the wet season, where the average maximum value is ≈ 0.92 m^2 s^{-2}. This result is in agreement with those obtained by Omokungbe et al. (2022), who found relatively lower TKE during a month of intense rainfall compared to the TKE of other months they studied in a tropical region in Nigeria. Mamtimin et al. (2021) also found that TKE is lower in winter at a site in the Gurbantünggüt Desert in China.

The relatively lower daytime insolation and wind speed during the wet season (Figs. 1a and 2) results, respectively, in lower Buoyancy and Shear productions compared to other periods (Fig. 9d, f), given that they are the main sources of TKE (Wang et al. 2016; Tong et al. 2022). Figure 9c, e prove that they show a good correlation with TKE. During nighttime periods, the shear production (S) is practically the only contribution from the TKE since the buoyancy production (S) is small and negative (Fig. 9e). This may partly explain the low value of TKE during stable conditions.

The results of Barman et al. (2019) obtained from measurements at several altitudes on a plateau in India also show that the TKE increases during the day and becomes low during the night. Furthermore, the observations of these authors (Barman et al. 2019) show an increase in TKE with measurement height.

4.5 Turbulence Intensity

Figure 10 shows the variation of turbulence intensity along the three wind directions (u, v and w) with respect to U during the different seasons and transition phases and according to the stratification of the atmosphere. The turbulence intensities I_u, I_v and I_w decrease rapidly with

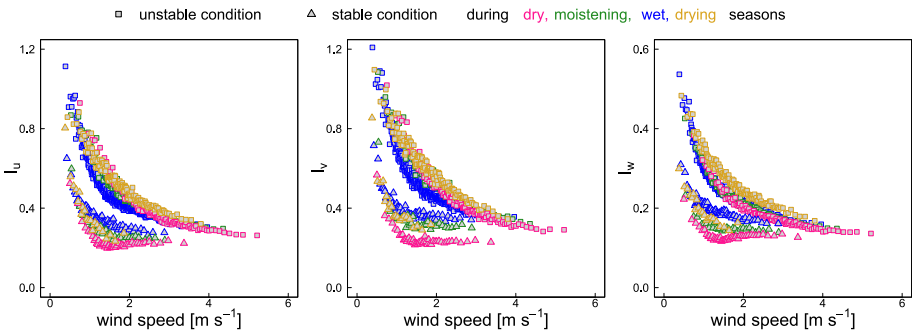

Fig. 10 Relationship between turbulence intensity and wind speed. The lightgray squares (respectively triangles) with pink, green, blue and gold borders represent the bin-averages (of 40 individuals) of the 30 min measurements during dry, moistening, wet and drying seasons, respectively, under unstable (respectively, stable) condition

increasing U and when it varies between 0 and ~ 2 m s^{-1} under unstable conditions and 0 and ~ 1 m s^{-1} under stable conditions (Fig. 10). However, when the wind speed becomes larger, the turbulence intensity in all three directions becomes almost constant (Fig. 10) consistent with the expectation of stability being more neutral. Similar results have been observed over other ecosystem types (Jia et al. 2017; Jiang et al. 2021; Mamtimin et al. 2021; Omokungbe et al. 2022).

Under unstable conditions, the average turbulence intensities are equal to 0.47, 0.54 and 0.23 following the u, v and w directions, respectively. Lower average values ($I_u = 0.31$, $I_v = 0.34$ and $I_w = 0.17$) are, however, observed under stable condition. Similar to the flux-variances similarity functions, turbulence intensities vary with the season. Following all directions, it is lowest in the dry season. This could be explained by the frequency of high wind speeds observed during this season compared to other periods. Overall, on average, whatever the season and atmospheric stability condition at the studied site, $I_u = 0.44$, $I_v = 0.50$ and $I_w = 0.22$ ($I_u \approx I_v > I_w$).

5 Summary and Conclusion

The critical value of the flux Richardson number, the similarity functions, turbulence kinetic energy (TKE) and turbulence intensities were analyzed in this study over a heterogeneous cultivated area located in West Africa and using long-term eddy covariance measurements (2007–2013). The results show an increase and decrease in TKE due to the different production and consumption terms of its budget. Thermal production due to buoyancy related to the temperature gradient and mechanical production due to wind shear increase in the daytime, resulting in maximum kinetic energy thus favouring turbulent transfers in the ABL. TKE is relatively low and nearly constant at night due to the relatively weaker winds at night and the absence of solar radiation. During these periods when the atmosphere is stable, a finite asymptotic value approximately equal to 0.17 of the flux Richardson number was observed when the stability parameter becomes very large. Below this critical value, the flow is or becomes turbulent. Results also show that the turbulence intensity is more important in unstable conditions, during which all turbulent fluxes reach their maximum. When the wind speed becomes high, turbulence intensity becomes constant. The average values obtained are 0.44, 0.50 and 0.22 following the directions u, v and w of the wind speed, respectively.

In accordance with the results of a previous study on a woodland forest in the same climatic zone as our study site, the similarity functions show a clear seasonal dependence, notably under stable condition, but all similarity functions (except $\phi_T(\zeta)$, which is a function of the stability parameter power -1 near-neutral conditions) obey MOST regardless of season and atmospheric stratification. Self-correlation effects caused by the friction velocity u_* have been observed on the similarity relationships, but those relationships explain well the physical processes of turbulence in unstable condition (except $\phi_q(\zeta)$). On the contrary, the self-correlation effect is less significant in stable stratification of the atmosphere, but the actual fraction of variance explained by physical processes is very low.

Finally, the differences obtained when comparing the similarity functions of the cultivated area and those of the woodland forest site, indicate that climatic conditions are not the major factors of these functions, although they are conditioning the development of atmospheric turbulence. All these findings suggest rather that the measurement height and the type of ecosystem (aerodynamic parameter) could be factors influencing atmospheric turbulence at the scale of this study.

Acknowledgements M.H. was financially supported by the PhD grant provided by the 'Ministère de l'Enseignement Supérieur et de la Recherche Scientifique', Bénin and the German Federal Ministry for Education through the German Academic Exchange Service (DAAD). H.M. would like to thank Biosystems Dynamics and Exchanges (BIODYNE) research axis of the Gembloux Agro-Bio Tech faculty of the University of Liege (Belgium) and ERASMUS + international relationship for funding the five-month internship at BIODYNE. The authors would like to thank the AMMA-CATCH observatory for collecting the data used in this study. The authors thank AuthorAID for editing the manuscript and the four anonymous reviewers for their fruitful and helpful comments. This work was carried out with the aid of a grant from UNESCO and the International Development Research Centre, Ottawa, Canada. The views expressed herein do not necessarily represent those of UNESCO, IRDC or its Board of Governors.

Author Contributions MH and OM conceptualized the manuscript, defined the methodology and analyses. MH prepared all figures and table and wrote the first draft of the manuscript. All authors wrote and reviewed the manuscript.

Data Availability https://doi.org/10.17178/AMMA-CATCH.AE.H2OFlux_Odc.

Declarations

Conflict of interest The authors declare no competing interests.

References

Afeti GM, Resch FJ (2000) Physical characteristics of Saharan dust near the Gulf of Guinea. Atmos Environ 34:1273–1279. https://doi.org/10.1016/S1352-2310(99)00296-4

Ago EE, Agbossou EK, Galle S et al (2014) Long term observations of carbon dioxide exchange over cultivated savanna under a Sudanian climate in Benin (West Africa). Agric Meteorol 197:13–25. https://doi.org/10.1016/J.AGRFORMET.2014.06.005

Arya SPS (1972) The critical condition for the maintenance of turbulence in stratified flows. Q J R Meteorol Soc 98:264–273. https://doi.org/10.1002/qj.49709841603

Aubinet M, Vesala T, Papale D (2012) Eddy Covariance, A Practical Guide to Measurement and Data Analysis. Springer Atmospheric Sciences

Babić K, Rotach MW, Klaić ZB (2016a) Evaluation of local similarity theory in the wintertime nocturnal boundary layer over heterogeneous surface. Agric Meteorol 228–229:164–179. https://doi.org/10.1016/j.agrformet.2016.07.002

Babić N, Večenaj Ž, De Wekker SFJ (2016b) Flux-variance similarity in complex terrain and its sensitivity to different methods of treating non-stationarity. Boundary-Layer Meteorol 159:123–145. https://doi.org/10.1007/s10546-015-0110-0

Barman N, Borgohain A, Kundu SS et al (2019) Daytime temporal variation of surface-layer parameters and turbulence kinetic energy budget in topographically complex terrain around Umiam, India. Boundary-Layer Meteorol 172:149–166. https://doi.org/10.1007/S10546-019-00443-6

Barskov K, Chechin D, Drozd I et al (2022) Relationships between second and third moments in the surface layer under different stratification over grassland and urban landscapes. Boundary-Layer Meteorol. https://doi.org/10.1007/s10546-022-00751-4

Basu S, Porté-agel F, Foufoula-Georgiou E et al (2006) Revisiting the local scaling hypothesis in stably stratified atmospheric boundary-layer turbulence: an integration of field and laboratory measurements with large-eddy simulations. Boundary-Layer Meteorol 119:473–500. https://doi.org/10.1007/s10546-005-9036-2

Bou-Zeid E, Gao X, Ansorge C, Katul GG (2018) On the role of return to isotropy in wall-bounded turbulent flows with buoyancy. J Fluid Mech 856:61–78. https://doi.org/10.1017/jfm.2018.693

Brutsaert W (1982) The surface roughness parameterization. Evaporation into the Atmosphere. pp 113–127

Doukouré M (2011) Variabilité des flux turbulents de surface au sein du bassin versant d'Ara au Bénin. Université de Grenoble

Ellison TH (1957) Turbulent transport of heat and momentum from an infinite rough plane. J Fluid Mech 2:456. https://doi.org/10.1017/S0022112057000269

FAO (2022) FRA 2020 remote sensing component. FAO Forestry Paper No. 186. Rome
Foken T (2017) Micrometeorology, 2nd edn. Springer, Berlin Heidelberg
Foken T, Wichura B (1996) Tools for quality assessment of surface-based flux measurements. Agric for Meteorol 78:83–105. https://doi.org/10.1016/0168-1923(95)02248-1
Fortuniak K, Pawlak W, Siedlecki M (2013) Integral turbulence statistics over a central European city centre. Boundary-Layer Meteorol 146:257–276. https://doi.org/10.1007/s10546-012-9762-1
Freire LS, Chamecki M, Bou-Zeid E, Dias NL (2019) Critical flux Richardson number for Kolmogorov turbulence enabled by TKE transport. Q J R Meteorol Soc 145:1551–1558. https://doi.org/10.1002/qj.3511
Grachev AA, Andreas EL, Fairall CW et al (2007) SHEBA flux-profile relationships in the stable atmospheric boundary layer. Boundary-Layer Meteorol. https://doi.org/10.1007/s10546-007-9177-6
Grachev AA, Andreas EL, Fairall CW et al (2013) The critical richardson number and limits of applicability of local similarity theory in the stable boundary layer. Boundary-Layer Meteorol 147:51–82. https://doi.org/10.1007/s10546-012-9771-0
Guyot A, Cohard J, Anquetin S, Galle S (2012) Agricultural and Forest Meteorology Long-term observations of turbulent fluxes over heterogeneous vegetation using scintillometry and additional observations : a contribution to AMMA under Sudano-Sahelian climate. Agric for Meteorol 154–155:84–98. https://doi.org/10.1016/j.agrformet.2011.10.008
Guzha AC, Rufino MC, Okoth S et al (2018) Impacts of land use and land cover change on surface runoff, discharge and low flows: evidence from East Africa. J Hydrol Reg Stud 15:49–67. https://doi.org/10.1016/J.EJRH.2017.11.005
Hounsinou M, Mamadou O, Wudba M et al (2022) Integral turbulence characteristics over a clear woodland forest in northern Benin (West Africa). Atmos Res 268:105985. https://doi.org/10.1016/j.atmosres.2021.105985
Hurdebise Q, Heinesch B, De Ligne A et al (2017) Impact of canopy aerodynamic distance spatial and temporal variability on long term eddy covariance measurements. Agric for Meteorol 247:131–138. https://doi.org/10.1016/J.AGRFORMET.2017.07.013
Jia D, Wen J, Ma Y et al (2017) The warm season characteristics of the turbulence structure and transfer of turbulent kinetic energy over alpine wetlands at the source of the Yellow River. Meteorol Atmos Phys 130:529–542. https://doi.org/10.1007/s00703-017-0534-9
Jiang J, Gao X, Chen B (2021) The impact of utility-scale photovoltaics plant on near surface turbulence characteristics in gobi areas. Atmosphere 12:1–14. https://doi.org/10.3390/atmos12010018
Kaimal JC, Finnigan JJ (1994) Atmospheric Boundary Layer Flows: their structure and measurement. Oxford University Press, New York
Kalapureddy MCR, Kishore Kumar K, Sivakumar V et al (2007) Diurnal and seasonal variability of TKE dissipation rate in the ABL over a tropical station using UHF wind profiler. J Atmos Solar-Terrestrial Phys 69:419–430. https://doi.org/10.1016/j.jastp.2006.10.016
Kent CW, Grimmond S, Barlow J et al (2017) Evaluation of urban local-scale aerodynamic parameters : implications for the vertical profile of wind speed and for source Areas. Boundary-Layer Meteorol. https://doi.org/10.1007/s10546-017-0248-z
Klipp CL, Mahrt L (2004) Flux-gradient relationship, self-correlation and intermittency in the stable boundary layer. Q J R Meteorol Soc 130:2087–2103. https://doi.org/10.1256/qj.03.161
Kljun N, Calanca P, Rotach MW, Schmid HP (2015) A simple two-dimensional parameterisation for flux footprint prediction (FFP). Geosci Model Dev 8:3695–3713. https://doi.org/10.5194/gmd-8-3695-2015
Kondo J, Kanechika O, Yasuda N (1978) Heat and momentum transfers under strong stability in the atmospheric surface layer. J Atmos Sci. https://doi.org/10.1175/1520-0469(1978)035%3c1012:HAMTUS%3e2.0.CO;2
Lambin EF, Geist HJ, Lepers E (2003) Dynamics of land-use and land-cover change in tropical regions. Annu Rev Environ Resour 28:205–246. https://doi.org/10.1146/annurev.energy.28.050302.105459
Liu Y, Liu HZ, Wang L (2017) The vertical distribution characteristics of integral turbulence statistics in the atmospheric boundary layer over an urban area in Beijing. Sci China Earth Sci 60:1533–1545. https://doi.org/10.1007/s11430-016-9050-5
Lohou F, Saïd F, Lothon M et al (2010) Impact of boundary-layer processes on near-surface turbulence within the West African monsoon. Boundary-Layer Meteorol 136:1–23. https://doi.org/10.1007/s10546-010-9493-0
Lothon M, Saïd F, Lohou F, Campistron B (2008) Observation of the diurnal cycle in the low troposphere of West Africa. Mon Weather Rev 136:3477–3500. https://doi.org/10.1175/2008MWR2427.1

Mahrt L (1999) Stratified atmospheric boundary layers. Boundary-Layer Meteorol 90:375–396. https://doi.org/10.1023/A:1001765727956

Mahrt L (2014) Stably stratified atmospheric boundary layers. Annu Rev Fluid Mech 46:23–45. https://doi.org/10.1146/annurev-fluid-010313-141354

Mamadou O, Cohard JM, Galle S et al (2014) Energy fluxes and surface characteristics over a cultivated area in Benin: daily and seasonal dynamics. Hydrol Earth Syst Sci 18:893–914. https://doi.org/10.5194/hess-18-893-2014

Mamadou O, Galle S, Cohard JM et al (2016) Dynamics of water vapor and energy exchanges above two contrasting Sudanian climate ecosystems in Northern Benin (West Africa). J Geophys Res 121:11269–11286. https://doi.org/10.1002/2016JD024749

Mamadou O (2014) Etude des flux d'Evapotranspiration en climat soudanien: comportement comparé de deux couverts végétaux au Bénin. Université de Grenoble (France) et Université d'Abomey-Calavi (Bénin), Abomey-Calavi

Mamtimin A, Wang Y, Sayit H et al (2021) Characteristics of turbulence over the semi-fixed desert area north of Xinjiang, China. Earth Surf Process Landforms 46:2365–2378. https://doi.org/10.1002/esp.5182

Martano P (2000) Estimation of surface roughness length and displacement height from single-level sonic anemometer data. J Appl Meteorol 39:708–715. https://doi.org/10.1175/1520-0450(2000)039%3c0708:EOSRLA%3e2.0.CO;2

Moraes OLL, Acevedo OC, Degrazia GA et al (2005) Surface layer turbulence parameters over a complex terrain. Atmos Environ 39:3103–3112. https://doi.org/10.1016/j.atmosenv.2005.01.046

Nadeau DF, Pardyjak ER, Higgins CW, Parlange MB (2013) Similarity scaling over a steep alpine slope. Boundary-Layer Meteorol 147:401–419. https://doi.org/10.1007/s10546-012-9787-5

Namdev P, Sharan M, Mishra SK (2022) Impact of the similarity functions of surface layer parametrization in a climate model over the Indian region. Q J R Meteorol Soc. https://doi.org/10.1002/QJ.4400

Omokungbe OR, Olufemi AP, Ayoola MA et al (2022) Statistics of atmospheric surface layer turbulence over a tropical region: a case study of Ile-Ife, Nigeria. Model Earth Syst Environ. https://doi.org/10.1007/s40808-022-01496-2

Pahlow M, Parlange MB, Porté-Agel F (2001) On Monin-Obukhov similarity in the stable atmospheric boundary layer. Boundary Layer Metrol. https://doi.org/10.1023/A:1018909000098

Panofsky HA, Dutton JA (1984) Atmospheric turbulence: models and methods for engineering applications. New York

Pellarin T, Tran T, Cohard JM et al (2009) Soil moisture mapping over West Africa with a 30-min temporal resolution using AMSR-E observations and a satellite-based rainfall product. Hydrol Earth Syst Sci 13:1887–1896. https://doi.org/10.5194/HESS-13-1887-2009

Rodrigo JS, Anderson PS (2013) Investigation of the stable atmospheric boundary layer at Halley Antarctica. Boundary-Layer Meteorol 148:517–539. https://doi.org/10.1007/s10546-013-9831-0

Rogachevskii I, Kleeorin N, Zilitinkevich S (2021) Unified theory for surface layers in atmospheric convective and stably stratified turbulence. arXiv. https://doi.org/10.48550/arXiv.2112.14121

Rotach MW (1994) Determination of the zero plane displacement in an urban environment. Boundary-Layer Meteorol 67:187–193. https://doi.org/10.1007/BF00705513

Stull RB (1988) An introduction to boundary layer meteorology. Kluwer Acic Publishers, Dordrecht

Sun J, Nappo CJ, Mahrt L et al (2015) Review of wave-turbulence interactions in the stable atmospheric boundary layer. Rev Geophys. https://doi.org/10.1002/2015RG000487

Toda M, Sugita M (2003) Single level turbulence measurements to determine roughness parameters of complex terrain. J Geophys Res Atmos 108:1–9. https://doi.org/10.1029/2002JD002573

Tong B, Guo J, Wang Y et al (2022) The near-surface turbulent kinetic energy characteristics under the different convection regimes at four towers with contrasting underlying surfaces. Atmos Res. https://doi.org/10.1016/j.atmosres.2022.106073

Tsai J, Tsuang B (2005) Aerodynamic roughness over an urban area and over two farmlands in a populated area as determined by wind profiles and surface energy flux measurements. Agric for Meteorol 132:154–170. https://doi.org/10.1016/j.agrformet.2005.07.008

Wang Y, Xu X, Liu H et al (2016) Analysis of land surface parameters and turbulence characteristics over the Tibetan Plateau and surrounding region. J Geophys Res 121:9540–9560. https://doi.org/10.1002/2016JD025401

Zeng Z, Estes L, Ziegler AD et al (2018) Highland cropland expansion and forest loss in Southeast Asia in the twenty-first century. Nat Geosci 11:556–562. https://doi.org/10.1038/s41561-018-0166-9

Zeng Z, Wang D, Yang L et al (2020) Deforestation-induced warming over tropical mountain regions regulated by elevation. Nat Geosci 14:23–29. https://doi.org/10.1038/s41561-020-00666-0